PCCP

Accepted Manuscript

ROYAL SOCIETY OF CHEMISTRY

www.rsc.org/pccp

PCCP

PAPER

New insights into the thermal behaviour of organic ionic plastic crystals: magnetic resonance imaging of polycrystalline morphology alterations induced by solid-solid phase transitions

Received 00th January 20xx,
Accepted 00th January 20xx

DOI: 10.1039/x0xx00000x

www.rsc.org/

Konstantin Romanenko,*[a] Jennifer M. Pringle,[a,b] Luke A. O'Dell,[a] and Maria Forsyth,[a,b]

Organic ionic plastic crystals (OIPCs) show strong potential as solid-state electrolytes for lithium battery applications, demonstrating promising electrochemical performance and eliminating the need for a volatile and flammable liquid electrolyte. The ionic conductivity (σ) in these systems has recently been shown to depend strongly on polycrystalline morphology, which is largely determined by the sample's thermal history. [K. Romanenko et al., J. Am. Chem. Soc., 2014, 136, 15638]. Tailoring this morphology could lead to conductivities sufficiently high for battery applications, so a more complete understanding of how phenomena such as solid-solid phase transitions can affect the sample morphology is of significant interest. Anisotropic relaxation of nuclear spin magnetisation provides a new MRI based approach for studies of polycrystalline materials at both a macroscopic and molecular level. In this contribution, morphology alterations induced by solid-solid phase transitions in triisobutyl(methyl)phosphonium bis(fluorosulfonyl)imide ($P_{1444}FSI$) and diethyl(methyl)(isobutyl)phosphonium hexafluorophosphate ($P_{1224}PF_6$) are examined using magnetic resonance imaging (MRI), alongside nuclear magnetic resonance (NMR) spectroscopy, diffusion measurements and conductivity data. These observations are linked to molecular dynamics and structural behaviour crucial for the conductive properties of OIPCs. A distinct correlation is established between the conductivity at a given temperature, σ(T), and the intensity of the narrow NMR signal that is attributed to a mobile fraction, $f_m(T)$, of ions in the OIPC. To explain these findings we propose an analogy with the well-studied relationship between permeability (k) and void fraction (Θ) in porous media, with $k(\Theta)$ commonly quantified by a power-law dependence that can also be employed to describe σ(f_m).

Introduction

Organic ionic plastic crystals (OIPCs) are solids with charged molecules located on a periodic lattice but that can also feature local orientational and dynamic disorder, resulting in high plasticity. Properties such as non-flammability, low volatility, electrochemical and thermal stability, and high ionic conductivity make OIPCs attractive candidates for use in a variety of electrochemical devices.[1-8] As a result of their complex phase behaviour, commonly featuring one or more solid-solid phase transitions and the ability to form metastable phases, their ion transport properties can show a strong dependence on both temperature and thermal history.[9-11] The ion conduction is believed to occur via disordered regions such as extended crystallographic defects, dynamic heterogeneity, or grain boundaries, in which the ions show a higher level of mobility.[1,9-12] The preferential orientation of crystal grains can therefore result in macroscopically anisotropic conductivity with an enhanced value in the direction of alignment. We recently observed such alignment effects using magnetic resonance imaging (MRI) experiments, and showed that slowly cooling the triethyl(methyl)phosphonium bis(fluorosulfonyl)imide ($P_{1222}FSI$) from its melt state resulted in a preferred alignment of crystallites across the full volume of the sample, with a corresponding enhancement in conductivity of up to an order of magnitude.[11]

Conventional microscopy methods are unable to probe the interior 3D morphology of plastic materials and suffer from low structural contrast and destructive preparation procedures.[13] Magnetic resonance microscopy[14] and pulsed-field-gradient (PFG) diffusometry,[15] on the other hand, are

[a] Institute for Frontier Materials, Deakin University, Waurn Ponds Campus, 75 Pigdons Road, Geelong, Victoria 3220, Australia. E-mail:kroman@deakin.edu.au

[b] ARC Centre of Excellence for Electromaterials Science, Deakin University, Burwood Campus, 221 Burwood Highway, Burwood, Victoria 3125, Australia

intrinsically non-invasive and adaptable methodologies suitable for a variety of material studies.[16] Attention has recently been drawn to their strong potential for studying electrochemical systems in situ,[17-23] as well as for investigating plastic crystals electrolytes.[10,11]

MRI of solids is challenging due to short transverse relaxation time constants (T_2 and T_2*) which result in loss of resolution and sensitivity. OIPCs can exhibit T_2*'s as short as tens of microseconds, with NMR line widths exceeding 50 kHz. Pure phase encoding methods, such as Single Point Imaging (SPI)[24] and its rapid counterpart Single Point Ramped Imaging with T_1 Enhancement (SPRITE) can overcome these issues.[25]

The Centric Scan SPRITE[26,27] experiments have recently revealed a striking T_2* contrast anisotropy in molecular and ionic plastic crystals[11] providing a new conceptual approach for studies of polycrystalline solids. The transverse relaxation in a material demonstrating long range ordering of NMR interactions can depend on the direction of the external magnetic field (B_0).[28] Dipolar relaxation anisotropy has previously been reported for structurally anisotropic media such as tendon and cartilage tissues[29-32] and strained elastomers.[33] Other contributions to T_2* anisotropy can come from chemical shielding anisotropy (CSA), quadrupolar interactions and internal magnetic field gradients arising at the interface between regions with different magnetic susceptibility.

Since MRI is isotope-specific, it can readily distinguish between the cation and anion components of OIPCs. Here ^{1}H and ^{19}F SPRITE measurements reveal unique effects of solid-solid phase transitions on polycrystalline morphology, structure and dynamics in solid phases of diethyl(methyl)(isobutyl)phosphonium hexafluorophosphate ($P_{1224}PF_6$) and triisobutyl(methyl)phosphonium bis(fluorosulfonyl)imide ($P_{1444}FSI$). These OIPCs have earlier been characterised with conventional methods[7-9,34] and represent good model systems for novel solid state MRI studies as they exhibit multiple solid-solid phase transitions at easily accessible temperatures.

We also report a new empirical correlation between the measured ionic conductivity and the fraction of the OIPC mobile component determined by NMR, and propose an analogy with porous media that may help to understand the ion transport mechanisms occurring in these systems.

Experimental section

Sample Preparation

Diethyl(methyl)(isobutyl)phosphonium hexafluorophosphate ($P_{1224}PF_6$), triisobutyl(methyl)phosphonium bis(fluorosulfonyl)imide ($P_{1444}FSI$) and triethyl(methyl)phosphonium bis(fluorosulfonyl)imide ($P_{1222}FSI$) were prepared following procedures reported elsewhere.8 The OIPC samples were packed into 16 mm outer diameter (o.d.) glass vials. The sample A_1 was obtained by cooling $P_{1222}FSI$ from 100 °C (melting point, 47 °C) to 21 °C over 48 hours using a temperature controlled hot plate. The sample A_2 was obtained by cooling from the melt at ambient temperature.

Magnetic Resonance Imaging

MRI experiments were performed on a Bruker Avance-III system equipped with a 11.75 T vertical 89 mm bore magnet (500.07 MHz ^{1}H frequency), a water-cooled triaxial gradient set (Micro2.5) driven by three GREAT (1/60) amplifiers each providing 1.5 T m^{-1} maximum magnetic field gradient and Variable Temperature Control Unit BCU-II. The radio frequency (RF) excitation and MRI signal detection were achieved with birdcage resonators 25 mm i.d. (model MICWB40) operating at the Larmor frequencies of ^{1}H and ^{19}F.

Single point imaging (SPI)[24] and its rapid counterpart SPRITE[25-27] are suitable for artefact-free MRI of solids.[23,35,36] In a typical SPRITE acquisition protocol the imaging gradients are incremented with a millisecond repetition period, *TR*. Each increment is followed by a gradient stabilisation interval, a hard low flip angle (α) RF pulse, phase encoding time (T_P) and signal sampling. A few complex points of the Free Induction Decay (FID) signal per gradient step are acquired. Limited gradient strength and finite RF probe "dead time" dictate the minimum T_P to be a few tens of microseconds. Custom SPRITE pulse sequences were designed under the Bruker ParaVision environment. The k-space sampling strategy: centrically ordered sectoral interleaves cover a square region in the transverse plane (k_x-k_y) at a fixed k_z vector.[23] The imaging gradient is incremented linearly along k_z. Different numbers of interleaves can be used depending on required resolution and experiment duration.

The SPRITE protocol employed radio-frequency (RF) pulses 2 to 3 μs long (α ≈ π/40), *TR* of 1.3 ms, T_P of 68 μs, four sectoral interleaves and a matrix size of 37 × 37. The magnetisation recovery delay (≈ 5 T_1) varied from 2 to 5 s. The maximum gradient amplitude at the k-space periphery was 0.7 T m^{-1}. Eight complex data points of the FID per gradient step were sampled with a dwell time of 4 μs. The signal-to-noise ratio (SNR) was improved by averaging of four FID points. For each of these points the field of view (FOV) was scaled using the Chirp z-Transform algorithm.[27] The MRI experiment duration varied from 40 to 200 min per 3D image depending on the number of signal averages (NA = 8, 16 or 32) and the sample T_1. The MRI and NMR data were processed using Matlab (R2014b, The MathWorks, Inc).

The parameters of the PFG stimulated echo (STE) experiments were: effective duration of the gradient (δ), 3 ms; STE interval (τ), 5.5 ms; observation z-storage interval (Δ), 10 - 300 ms; NA, 8; π/2 pulse widths, 32 μs. The motion sensitising gradient amplitude of 2 T m^{-1} was achieved by combining X and Y gradients of the triaxial gradient coil.

The phase transitions in $P_{1444}FSI$ and $P_{1224}PF_6$ samples were confirmed by a sharp change in ^{19}F and ^{1}H NMR line widths. ^{1}H SPRITE sensitivity was sufficient only in phases I to III of $P_{1224}PF_6$ but it was ultimately low in phase IV due to shorter ^{1}H signal lifetime (T_2* < 20 μs). High fluorine density and moderate ^{19}F NMR line widths (< 13 kHz) provided a

favourable ^{19}F SPRITE sensitivity in all four phases of $P_{1224}PF_6$. However, due to the hardware temperature limitations only phases III and IV could be observed.

Results and discussion

SPRITE imaging of polycrystalline morphology

^{1}H, ^{19}F, and ^{31}P NMR spectroscopy studies of OIPCs have shown strong line width variations across different solid phases, indicating characteristic changes in ion dynamics.[9] For spin-1/2 nuclei the transverse magnetisation relaxation rate (R_2) can be contributed to by several anisotropic magnetic interactions:[28] dipolar couplings and chemical shielding anisotropy (CSA) (R_D and R_{CSA}, respectively) as well as internal magnetic field gradients arising from magnetic susceptibility variations, R_{IG}.[37,38] Thus for solids the Centric Scan SPRITE intensity $I(r)$ can be defined in a general form:

$$I(r)=\rho(r)\cdot F(R_2,T_P,\alpha) \quad (1)$$

Here, ρ(r) is the nuclear spin density and F is the magnetisation attenuation function, i.e. FID, time T_P after the excitation. In the general case, the FID is a complex function involving multiple non-exponential terms. In the case of a Lorentzian lineshape, FID is an exponential decay:[26,38]

$$F = \exp(-T_P / T_2^*) \sin(\alpha) \quad (2)$$

Note that short T_2* values affects the sensitivity but not the resolution of the SPRITE method. Equations (1) and (2) serve as a basis for MRI visualisation of polycrystalline morphology in solids.

Since the relaxation rate depends on the orientation of the crystallites with respect to B_0 one should expect an anisotropic SPRITE contrast. The anisotropy of magnetic interactions can be partially or fully averaged out by molecular dynamics and static orientational disorder. Given that molecular dynamics is not isotropic the anisotropic T_2* contrast can be observed if the size of the grains is on the order of the MRI voxel size or larger, or if a certain degree of alignment is present on a sub-voxel scale.

The T_2* sensitive SPRITE experiments performed at different temperatures and sample orientations can potentially provide unique information on activated modes of molecular motion and extent of static orientational disorder. Since $R_{IG} \sim B_0$ this contribution can be distinguished from R_D and R_{CSA} and estimated by NMR measurements performed in different magnetic fields.

Fluorine is a common element in many novel OIPCs electrolytes.[8] The high gyromagnetic ratio and 100% natural abundance of the ^{19}F isotope are favourable for sensitive ^{19}F MRI measurements. Here we demonstrate for the first time that the effects of ^{19}F CSA can be employed to visualize polycrystalline morphology in plastic crystals. The impact of thermal treatment on crystal grain alignment has been examined earlier in the P_{1222}FSI system with ^{1}H SPRITE imaging.[11] Cooling P_{1222}FSI from the melt at a sufficiently slow rate resulted in alignment of crystal grains throughout the entire sample. ^{19}F NMR spectra measured from the slowly cooled P_{1222}FSI sample (A_1) at several different orientations with respect to B_0 are displayed in Figure 1a in magnitude mode. The observed lineshape modulation is due to the ^{19}F chemical shielding anisotropy.

This result provides evidence for long range structural ordering in the anion sublattice with two ^{19}F CSA tensor orientations as would be expected from the two fluorine sites on the FSI anion. The widths of the two peaks vary within the range from 9 to 18 kHz. This is likely due to anisotropic broadening from hetero-nuclear dipolar interactions ^{1}H -^{19}F.

The ^{19}F SPRITE image intensity obtained from this sample was uniform, indicating no spatial variation of these CSA orientations.

The ^{19}F SPRITE image of the rapidly cooled P_{1222}FSI sample (A_2) shows polycrystalline texturing manifested through anisotropic T_2* contrast (≈ 20:1), Figure 2a. This contrast is induced by macroscopic domains with different ^{19}F CSA tensor orientations. The ^{19}F T_2* anisotropy is evident from the comparison of images of the vertically oriented and tilted sample (Figure 2a, Y-Z and Y-Z tilted). The signal visible in the lower right region of the ^{1}H image (Figure 2b, Y-Z tilted) results from a piece of Plasticine used to support the sample in the tilted position.

Note that since the shape of the magnitude-mode ^{19}F FIDs varies with the orientation of the domain (Figure 1b) the ^{19}F SPRITE image morphology is dependent on T_P (Equation 1). A series of complex SPRITE images acquired at different T_P's and Fourier transformed along the time dimension will provide the spatially resolved NMR spectrum. Although this approach would be quite time consuming, such variable T_P ^{19}F Centric Scan SPRITE measurements would allow the CSA tensor parameters to be mapped.

The respective T_2* contrast of the cation sublattice is shown in Figure 2b. Since the chemical shielding anisotropy in hydrogen is insignificant, the ^{1}H image intensity is mainly affected by dipolar couplings and potentially internal gradients created at the grain boundaries. In the case of P_{1222}FSI, R_{IG} contributes less than 3 kHz to overall line broadening at 11.75 T as estimated by comparison with the line width observed at 7.05 T.

A correlation between the ^{1}H and ^{19}F SPRITE image morphologies is readily noticeable, with domain boundaries extending inwards from the container walls in a radial conformation and indicating the direction of crystal growth that occurred during solidification. The local ^{1}H SPRITE intensity is determined largely by the magnitude of the dipolar interactions (^{1}H-^{1}H and ^{1}H-^{19}F) while the ^{19}F signal is dominated by the CSA lineshape.

OIPC morphology alterations induced by solid-solid phase transitions

The differential scanning calorimetry (DSC) traces of $P_{1444}FSI$ and $P_{1224}PF_6$ show sharp solid-solid phase transitions.[9,34] The diffusion length scale for the mobile cations in phase I of $P_{1222}FSI$ was previously shown to decrease with faster cooling rates from the melt.[11] Solid-solid phase transitions can also affect the ion transport via an accompanying re-crystallisation processes that affects the OIPC morphology. The phase transitions observed here occur over a macroscopic volume on a timescale of seconds. The 3D SPRITE imaging experiments therefore cannot provide sufficient temporal resolution to monitor rapid phase transitions as they occur. However, the image morphology alterations induced by the phase transitions can be easily detected and are extremely informative.

A. *$P_{1444}FSI$*

The thermal phase behaviour of triisobutyl(methyl)phosphonium bis(fluorosulfonyl)imide ($P_{1444}FSI$) and its associated electrochemical properties have previously been characterised with DSC and electrochemical techniques, respectively.[34]

The ^{1}H NMR spectra of the $P_{1444}FSI$ sample show two distinct components: a broad peak that varies in width depending on the phase and constitutes the majority of the signal intensity (≈ 99 %), and a much narrower line (FWHM ≈ 1.5 kHz) whose width does not vary significantly but whose relative intensity is temperature dependent (Figure 3). As suggested earlier[10,11] the narrow component arises from mobile species existing within grain boundary regions of the OIPC.

The $P_{1444}FSI$ system shows two solid-solid phase transitions and a melt transition, and their associated temperatures and the ^{1}H NMR line width of the broad component for each phase are shown in Table 1.

Table 1. Solid phases of $P_{1444}FSI$ and associated parameters

$P_{1444}FSI$	^{1}H $\Delta\nu_{1/2}$ (kHz)	Transition T(°C)[34]
III	40 (0 °C)	8.3 (III-II)
II	16.5 (18 °C)	24.2 (II-I)
I	7.5 (36 °C)	37.1 (I–melt)

The ^{1}H SPRITE sensitivity is favourable in all three phases. However, the relatively low density of fluorine and its strong chemical shift anisotropy in $P_{1444}FSI$ (≈ 100 kHz compared with approximately 50 kHz for $P_{1222}FSI$) resulted in a poorer sensitivity for the ^{19}F SPRITE measurements (data not shown).

MRI images were acquired from a $P_{1444}FSI$ sample as it was brought through its various solid phases in the following sequence: Melt (50 °C) → I(28 °C) → II(18 °C) → III(6 °C) → II(18 °C) → I(28 °C) → II(18 °C) → I(28 °C). The phase transitions were confirmed to have occurred via the observed rapid changes in the ^{1}H NMR line width (broad component). The sample was equilibrated for 12 hours after each transition before each image was recorded.

Figure 4a shows representative longitudinal slices (X-Z and Y-Z) through the 3D ^{1}H SPRITE image of the $P_{1444}FSI$ sample in phase I. The image remained largely constant over the temperature range of phase I with only minor (≈ 3 %) variation of the contrast due to changes in the intensity of the narrow NMR component. Relatively large domains of uniform signal intensity can be seen, each exhibiting preferential alignment as previously observed and discussed for the $P_{1222}FSI$ system.[11]

The transition from phase I to phase II entirely changed the image, indicating re-crystallisation throughout the sample volume (Figure 4a, b). The overall image intensity drops significantly in comparison to phase I due to a decrease in T_2*, however, the image contrast is also noticeably different with a larger number of domains visible. This difference can only be caused by physical changes in the polycrystalline domain structure, indicating that this phase transition involves a recrystallisation mechanism and a change in the lattice parameters. The resulting image features were found to be temperature-independent over the phase II region.

The next transition, from phase II to phase III (Figure 4 b, c), resulted in only minor changes in the image features and contrast, with the most significant difference being a decrease in overall signal intensity (Figure 4c). This transition therefore appears to involve a change in the rotational dynamics of the ions within the grains without a re-crystallisation to a new lattice type.

These dramatic differences in how the two solid-solid phase transitions affect the polycrystalline morphology of the OIPC also hold true upon heating. The transition III → II (Figure 4c, d) completely restored the image contrast previously observed in phase II (b). The images (b) and (d) are different only within the noise level (SNR ≈ 2.5 %). Going from II to I (Figure 4d, e) resulted in a completely new contrast, which it should be noted is markedly different to the original phase I contrast (Figure 4a). Cooling back to phase II once again gives rise to a unique image morphology (Figure 4f). The transition between phases I and II therefore causes irreversible changes in OIPC texturing, while the transition II ↔ III does not.

The transition I ↔ II involves a substantial alteration of the OIPC structure, not just a variation in the degree of rotational freedom of the ions. This could be due to the nucleation and growth of a new lattice structure, perhaps due to the onset of a new dynamic mode in phase I that requires a larger free volume in the structure. Conversely, phases II and III likely differ only in the rotational degree of freedom of the ions but not the lattice structure, since the II ↔ III phase transition results in no change in the overall morphology of the sample.

As we have demonstrated earlier[11] the ionic conductivity in these systems is strongly dependent on the extent of alignment of the crystal grains. Therefore, such fundamental differences between phase transition behaviours will be of huge importance for improved electrolyte materials design.

B. *$P_{1224}PF_6$*

Figure 5 displays the evolution of the ^{19}F SPRITE image observed in phases III and IV of $P_{1224}PF_6$ as the sample was brought through the following sequence of phases: Melt (150 °C) → I (125 °C) → II (100 °C) → III (30 °C) → IV (16 °C) → III (30 °C) → IV (16 °C). The sample was equilibrated for 12 hours after each transition. Table 2 lists NMR the line widths of the broad component and the phase transition temperatures.

Table 2. Solid phases of $P_{1224}PF_6$ and associated parameters

$P_{1224}PF_6$	^{19}F $\Delta\nu_{1/2}$ (kHz)	^{1}H $\Delta\nu_{1/2}$ (kHz)	Transition T (°C)[9]
IV	12	39 (0 °C)	25 (IV-III)
III	8	13 (30 °C)	70 (III-II)
II	2	7 (100 °C)	120 (II-I)
I	1.3	< 2.5	150 (I -melt)

The initial ^{19}F SPRITE image of $P_{1224}PF_6$ in phase III shows distinct macroscopic structures formed upon cooling from the melt, Figure 5a. This MRI contrast vanishes following the III → IV transition (step a - b). In phase IV, some intensity variation can be seen near the centre of the sample volume. These differences in MRI contrast during the III to IV transition were accompanied by changes in the visual appearance of the sample, with the initially translucent, coarse grained phase III sample changing into an opaque white and fine-grained appearance in phase IV. The IV → III transition (step b - c) led to an overall increase in image intensity (i.e. decreased line width) without noticeable changes either in contrast or in morphology. The transition III → IV (step c - d) resulted in overall intensity decrease but no change in morphology.

Image alterations associated with the phase III to II transition were also investigated using the following sequence of transitions: melt (150 °C) → I (125 °C) → II (100 °C) → III (30 °C) → II (100 °C) → III (30 °C). Domains observed in phase III (Figure 6a) were conserved after transitioning to phase II and back (Figure 6b).

It should noted that morphologies of anion (PF_6) and cation (P_{1224}) components are very similar (Figure 6, top - ^{19}F SPRITE, bottom - ^{1}H SPRITE). Since PF_6 is a highly symmetrical structure it can undergo rotational dynamics that average the CSA interaction. The R_{CSA} term is therefore small and ^{19}F SPRITE image is largely determined by inter-molecular dipolar interactions ^{19}F-^{1}H. Thus, the polycrystalline structure of $P_{1224}PF_6$ is seen to alter noticeably during the primary III → IV transition but is conserved during the III ↔ II and IV ↔ III transitions.

According to the most recent model of thermal behaviour in this system based on molecular dynamics simulations carried out over a range of temperatures,[39] in phase IV the anion undergoes isotropic rotation while the cation exhibits rotations of its methyl and ethyl groups. Upon transition to phase III the rotation of the butyl group is activated. In phase II, the cation undergoes a "crank shaft" mechanism while retaining its overall orientation. The transition to phase I activates the isotropic rotation of the cation, while the anion begins to undergo translational motion. Our experimental results are fully consistent with this model.

The conservation of the ^{1}H SPRITE image morphology in phase III after undergoing the transitions III → II → III (Figure 6) indicates that the cations experience limited degrees of freedom in both of these phases (e.g. rotation about a fixed axis) and that translational motion of the anion is unlikely in phase II. An earlier study[9] had proposed that within phase II the cation is rotating isotropically and the anion is diffusing. If this were the case, any memory of the cation orientation would be lost when transitioning back to phase III, resulting in a new orientation for the local interactions (Equation 1) and therefore a different image.

Conversely, the MRI results show that extensive changes occur during the primary III → IV transition (Figure 5a, b), resulting in increasing orientational disorder of grains and thus irreversibly erasing the phase III morphology. Subsequent IV → III → IV transitions did not change the image contrast, Figure 5b-d. This indicates that a stable low energy state has been reached with highly disordered grain packing.

Correlation between conductivity and the mobile fraction of OIPCs

Although the relatively high intrinsic ion conductivity in OIPCs is a well-known phenomenon, the ion transport mechanisms are still disputed in the literature.[1] The ^{1}H and ^{19}F NMR spectra obtained from $P_{1444}FSI$ as well as many other ionic salts tend to exhibit a narrow NMR component ($\Delta\nu_{1/2} \approx 1.5$ kHz) indicative of high mobility similar to that observed in the liquid state.[9, 11, 40-44] As mentioned above, these mobile species could exist within grain boundary regions, or as extended defect regions within the ordered lattice itself. In either case, due its high mobility this component can be safely assumed to mediate the ion transport.[11,12, 41-43]

A narrow ^{1}H NMR signal was observed from all the solid phases (T < 37 °C) of $P_{1444}FSI$ and its relative intensity was highly temperature dependent (although its line width was constant over the temperature range -4 to 37 °C). The mobile fractions, f_m, were obtained from ^{1}H NMR spectra intensity normalized by the intensity of the melt sample (Figure 7a). The broad ^{1}H NMR signals were filtered out by removing the first 260 µs of the FIDs.

Although the mobile component of the OIPC sample was small, its intensity variation with temperature exceeded two orders of magnitude before the melting point. The observed increase in this mobile fraction must be accompanied by a reduction of the immobile phase that can be interpreted as "melting" of the crystallites at the interface region, leading to an increase of the mobile domain.

The diffusion coefficients (D) measured from the mobile component also support these conclusions. Figure 8a shows

the results of variable temperature (VT) ^{1}H PFG STE experiments performed with a diffusion time (Δ) of 45 ms. The comparison of diffusive attenuations measured by Tanner[45] and Cotts[46] PFG schemes did not reveal any significant effects of internal magnetic field gradients in $P_{1444}FSI$.

The corresponding Arrhenius parameters for diffusion are: activation energy, E_a = 44 ± 1 kJ mol^{-1} and pre-exponential factor, D_0 = 2.5 ± 0.03×10^{-4} m^2 s^{-1}. The measured diffusion coefficients rapidly decrease with increasing Δ, asymptotically approaching constant values for longer Δ's, Figure 8b. This behaviour is due to restricted diffusion at Δ > 10 ms with a corresponding compartment size of less than 300 nm at 280 K, as estimated using Einstein's root-mean-square displacement $(2D\Delta)^{1/2}$.

Assuming that the mobile region exists as a continuous phase distinct from the immobile region (the crystallites), the ionic transport within it can be conceptualised based on an analogy with flow in porous media. The hydrodynamic permeability, *k*, is a measure of the capacity of a porous medium to conduct flow and can be considered as an analogue of ionic conductivity, σ.[36,47] On a quantitative level this is described by Darcy's law as a coefficient between fluid flux and pressure gradient, the counterparts of current density and electric field, respectively. In sedimentary rocks, permeability is a complex function of porosity (Θ), grain morphology and packing and can be anisotropic due to formation of bedding planes.[48,49] Permeability in homogeneous rocks is commonly discussed in terms of empirical power-law relationships, $k(\Theta)$.[50] Therefore, if the porous media model is applicable similar phenomenological behaviour can be expected for $\sigma(f_m)$, where f_m can be considered as a measure of the "porosity" of the OIPC. Here we use a power-law form $\sigma = \alpha f_m^{\beta}$ to quantify the correlation of σ and f_m.

Since the conductivity depends on thermal history[11] the measurements of σ and f_m should ideally be performed simultaneously. However, these two measurements both involve metal components (electrodes and NMR resonator, respectively) producing detrimental effects on one another. The OIPC samples discussed below were cooled from the melt on the time scale of seconds prior to the measurements of $f_m(T)$ and $\sigma(T)$. Rapid cooling does not lead to significant macroscopic crystal alignment effects[11] and provides highly reproducible conductivity measurements σ(T).

Figure 7b displays the conductivity of $P_{1444}FSI$ (measured using electrochemical impedance spectroscopy), log{σ(T)}, and the corresponding log{αf_m^{β}(T)}. These data sets were matched using least squares fitting, resulting in α = 0.0059 S cm^{-1} and β = 2.32. Note that within a capillary tube model permeability scales as porosity squared.[51]

Figure 9a shows log{σ(T)}, and log{f_m(T)} observed in $P_{1224}PF_6$. The parameters α and β were phase dependent: IV, $\sigma(f_m) \approx 3 f_m^3$; III, $\sigma(f_m) \approx 0.11 f_m^2$; II, $\sigma(f_m) \approx (24.7 f_m)^{16}$. In phase II the dependence $\sigma(f_m)$ was rather strong: a 10% increase in mobile fraction was accompanied by nearly an order of magnitude increase in conductivity.

In phase I of the $P_{1222}FSI$ sample the conductivity was approximated by $\sigma(f_m) = 3\times10^{-5} f_m^{0.88}$, Figure 9b. The coefficient α was found to vary by an order of magnitude depending on cooling rate, while β values were similar.

Given that a mobile fraction is observed in NMR experiments in the vast majority of highly conductive plastic crystals[9, 11, 40-44] our future work will examine the possibility that phenomenological relationships between σ and f_m are a general feature of OIPCs and may provide a means for controlling conductivity through design of this interconnected conduction pathway.

Conclusions

MRI has been shown to be a powerful method for the non-destructive imaging of polycrystalline solids, with unique capabilities to probe both the orientations and dynamics of the constituent molecules. In particular, the analysis of solid-solid phase transitions by imaging the changes in crystallite alignment and domain morphology is a novel strategy for understanding the thermal behaviour of plastic crystals and can provide a direct window into the molecular dynamics occurring in the various phases of these materials.

In the systems studied herein, while the fraction of the mobile component measured by NMR always continuously increases with temperature, the polycrystalline structure is stable within the temperature range of a given phase and can change abruptly during a phase transition. Depending on the nature of the solid-solid phase transition these morphology changes can be reversible or irreversible. In the latter case, the re-crystallisation to a new lattice structure causes irreversible alterations in the morphology, and this can be a crucial process determining the conductivity in OIPC-based solid electrolytes operating over a wide range of temperatures. MRI provides a detailed, spatially-resolved view of these two distinct transition types, which cannot be distinguished from DSC traces alone and are difficult to study by diffraction techniques due to the inherent disorder and dynamics present in these materials.

The thermal behaviour of ionic conductivity in OIPCs can be rationalised in terms of a mobile component with a temperature dependent volume fraction. We have proposed a potentially useful analogy with flow in anisotropic porous media. This model is supported by correlating the ionic conductivity with the mobile fraction of the OIPCs, the latter determined using conventional 1D NMR spectroscopy measurements. It is anticipated that the utilisation of magnetic resonance based techniques will further illuminate the role of thermal history, phase transitions and alignment effects in the transport properties of OIPCs and lithium and sodium doped OIPC electrolytes.

Acknowledgements

Dr. Liyu Jin is thanked for providing the conductivity data. The Australian Research Council is acknowledged for funding the Magnetic Resonance Facility through LIEF grant LE11010014 and for funding of the project through the Laureate Fellowship

Program FL110100013. Funding through the ARC Centre of Excellence for Electromaterials Science and the Deakin University Central Research Grants Scheme 2015 are also gratefully acknowledged.

Notes and references

1 J. M. Pringle, *Phys. Chem. Chem. Phys*., 2013, **15**, 1339-1351.
2 A. Abouimrane, Y. Abu-Lebdeb, P. J. Alarco and M. Armand, *J. Electrochem. Soc.*, 2004, **151**, A1028-A1031.
3 Y. Abu-Lebdeh, A. Abouimrane, P. J. Alarco, A. Hammami, L. Ionescu-Vasii and M. Armand, *Electrochem. Commun*., 2004, **6**, 432-434.
4 P. Wang, Q. Dai, S. M. Zakeeruddin, M. Forsyth, D. R. MacFarlane and M. Gratzel, *J. Am. Chem. Soc.*, 2004, **126**, 13590-13591.
5 V. Armel, M. Forsyth, D. R. MacFarlane and J. M. Pringle, *Energy Environ. Sci.*, 2011, **4**, 2234-2239.
6 L. Y. Jin, P.Efthimiadis, J.Kar, M.Macfarlane, D. R.Forsyth, M., *J. Mater. Chem*., 2011, **21**, 10171-10178.
7 J. Sunarso, Y. Shekibi, J. Efthimiadis, L. Y. Jin, J. M. Pringle, A. F. Hollenkamp, D. R. MacFarlane, M. Forsyth and P. C. Howlett, *J. Solid State Electrochem.*, 2012, **16**, 1841-1848.
8 V. Armel, D. Velayutham, J. Sun, P. C. Howlett, M. Forsyth, D. R. MacFarlane and J. M. Pringle, *J. Mater. Chem.*, 2011, **21**, 7640-7650.
9 L. Y. Jin, K. M. Nairn, C. M. Forsyth, A. J. Seeber, D. R. MacFarlane, P. C. Howlett, M. Forsyth and J. M. Pringle, *J. Am. Chem. Soc.*, 2012, **134**, 9688-9697.
10 B. E. Kidd, M. D. Lingwood, M. Lee, H. W. Gibson and L. A. Madsen, *J. Phys. Chem. B*, 2014, **118**, 2176-2185.
11 K. Romanenko, L. Jin, L. A. Madsen, J. M. Pringle, L. A. O'Dell and M. Forsyth, *J. Am. Chem. Soc.*, 2014, **136**, 15638-15645.
12 F. Chen, S. W. de Leeuw and M. Forsyth, *J. Phys. Chem. Lett.*, 2013, **4**, 4085-4089.
13 G.H. Michler, *Electron Microscopy of Polymers*, Springer Verlag, Berlin, 2008.
14 P.T. Callaghan, *Principles of Nuclear Magnetic Resonance Microscopy*, Oxford University Press, Oxford, 1993.
15 W.S. Price, *NMR Studies of Translational Motion*, Cambridge University Press, Cambridge, 2009.
16 B. Blümich, *NMR Imaging of Materials*, Oxford University Press, Oxford, 2000.
17 B. Key, R. Bhattacharyya, M. Morcrette, V. Seznec, J.-M. Tarascon and C. P. Grey, *J. Am. Chem. Soc.*, 2009, **131**, 9239-9249.
18 R. Bhattacharyya, B. Key, H. Chen, A. S. Best, A. F. Hollenkamp and C. P. Grey, *Nat. Mater.*, 2010, **9**, 504-510.
19 S. Chandrashekar, N. M. Trease, H. J. Chang, L.-S. Du, C. P. Grey and A. Jerschow, *Nat. Mater.*, 2012, **11**, 311-315.
20 M. Klett, M. Giesecke, A. Nyman, F. Hallberg, R. W. Lindstrom, G. Lindbergh and I. Furo, *J. Am. Chem. Soc.*, 2012, **134**, 14654-14657.
21 S. A. Krachkoyskiy, A. D. Pauric, I. C. Halalay and G. R. Goward, *J. Phys. Chem. Lett.*, 2013, **4**, 3940-3944.
22 K. Ogata, E. Salager, C. J. Kerr, A. E. Fraser, C. Ducati, A. J. Morris, S. Hofmann and C. P. Grey, *Nat. Commun.*, 2014, **5**, 3217.
23 K. Romanenko, M. Forsyth and L. A. O'Dell, *J. Magn. Reson.*, 2014, **248**, 96-104.
24 S. Emid and J. H. N. Creyghton, Physica B & C, 1985, **128**, 81-83.
25 B. J. Balcom, R. P. MacGregor, S. D. Beyea, D. P. Green, R. L. Armstrong and T. W. Bremner, *J. Magn. Reson.* A, 1996, **123**, 131-134.
26 I. V. Mastikhin, B. J. Balcom, P. J. Prado and C. B. Kennedy, *J. Magn. Reson.*, 1999, **136**, 159-168.
27 M. Halse, J. Rioux, S. Romanzetti, J. Kaffanke, B. MacMillan, I. Mastikhin, N. J. Shah, E. Aubanel and B. J. Balcom, *J. Magn. Reson.*, 2004, **169**, 102-117.
28 A. Abragam, *Principles of Nuclear Magnetism*, Oxford University Press, Oxford, 1961.
29 S. J. Erickson, I. H. Cox, J. S. Hyde, G. F. Carrera, J. A. Strandt and L. D. Estkowski, *Radiology*, 1991, **181**, 389-392.
30 Y. Xia, *J. Magn. Reson. Imag.*, 2000, **11**, 686-693.
31 Y. Xia, J. B. Moody, H. Alhadlaq and J. N. Hu, *J. Magn. Reson.* Imag., 2003, **17**, 365-374.
32 H. A. Alhadlaq and Y. Xia, *J. Magn. Reson. Imag.*, 2005, **22**, 665-673.
33 K. Hailu, R. Fechete, D. E. Demco and B. Blumich, *Solid State Nucl. Magn. Reson.*, 2002, **22**, 327-343.
34 L. Jin, P. C. Howlett, J. M. Pringle, J. Janikowski, M. Armand, D. R. MacFarlane and M. Forsyth, *Energy Environ. Sci.*, 2014, **7**, 3352-3361.
35 K. V. Romanenko, P. F. d. J. Cano-Barrita and B. J. Balcom, *J. Magn. Reson.*, 2009, **198**, 24-30.
36 K. Romanenko and B. J. Balcom, *Aiche J.*, 2012, **58**, 3916-3926.
37 M. D. Hürlimann, *J. Magn. Reson.*, 1998, **131**, 232-240.
38 Q. Chen, A. E. Marble, B. G. Colpitts and B. J. Balcom, *J. Magn. Reson.*, 2005, **175**, 300-308.
39 F. Chen, L. Jin, S. W. de Leeuw, J. M. Pringle and M. Forsyth, *J. Chem. Phys.*, 2013, **138**, 244503.
40 H. A. Every, A. G. Bishop, D. R. MacFarlane, G. Oradd and M. Forsyth, *J. Mater. Chem.*, 2001, **11**, 3031-3036.
41 A. J. Seeber, M. Forsyth, C. M. Forsyth, S. A. Forsyth, G. Annat and D. R. MacFarlane, *Phys. Chem. Chem. Phys.*, 2003, **5**, 2692-2698.
42 J. Adebahr, A. J. Seeber, D. R. MacFarlane and M. Forsyth, *J. Appl. Phys.*, 2005, **97**, 5.
43 J. Adebahr, A. J. Seeber, D. R. MacFarlane and M. Forsyth, *J. Phys. Chem. B*, 2005, **109**, 20087-20092.
44 J. Adebahr, M. Grirnsley, N. M. Rocher, D. R. MacFarlane and M. Forsyth, *Solid State Ionics*, 2008, **178**, 1798-1803.
45 J. E. Tanner, *J. Chem. Phys.*, 1970, **52**, 2523-&.
46 R. M. Cotts, M. J. R. Hoch, T. Sun and J. T. Markert, *J. Magn. Reson.*, 1989, **83**, 252-266.
47 K. V. Romanenko and B. J. Balcom, *Exp. Fluids*, 2011, **50**, 301-312.
48 J. H. Baas, E. A. Hailwood, W. D. McCaffrey, M. Kay and R. Jones, *Earth-Sci. Rev.*, 2007, **82**, 101-142.
49 J. B. Clavaud, A. Maineult, M. Zamora, P. Rasolofosaon and C. Schlitter, *J. Geophys. Res.-Solid Earth*, 2008, **113**, 10.
50 S. Ma, N. R. Morrow, Proceedings from the International Symposium of the The Society of Core Analysts, Montpelier, 1996.
51 J.A. Fanchi, *Principles of Applied Reservoir Simulation*, Gulf Professional Publishing, Oxford, 2006.

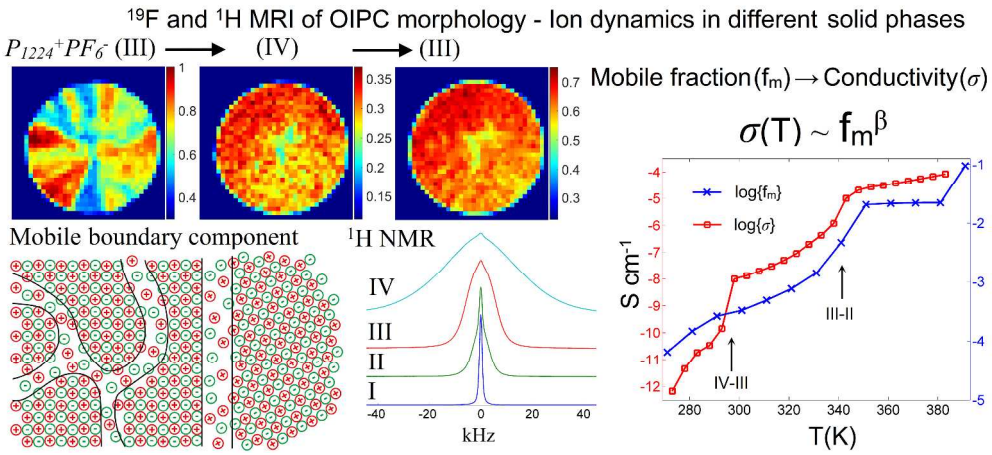

Graphical abstract
2135x953mm (96 x 96 DPI)

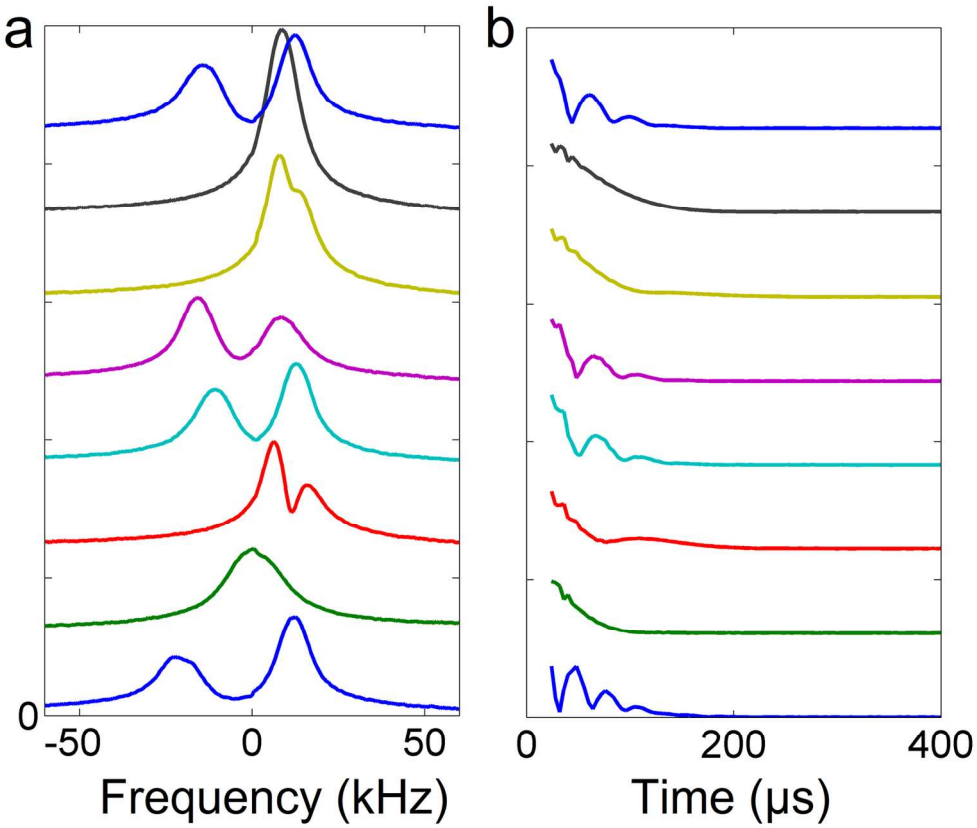

Figure 1. Static magnitude ^{19}F NMR lineshapes (a) and FID's (b) observed for the sample A_1 rotated about an axis perpendicular to B_0 with a 45° step; T = 18 °C.
151x127mm (300 x 300 DPI)

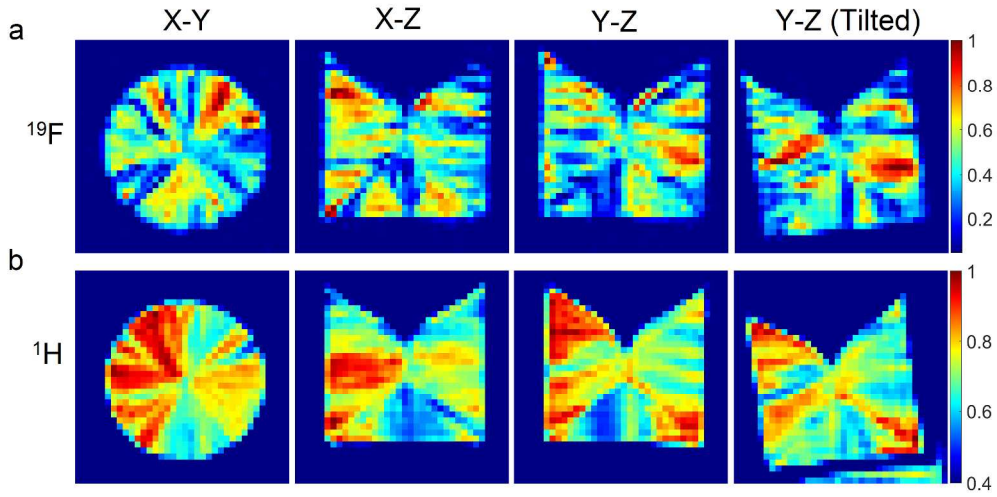

Figure 2. Representative slices (X-Y, X-Z and Y-Z) through 3D ^{19}F (a) and ^{1}H (b) SPRITE images of the sample A_2; FOV = 16×16 mm^2; T = 18 °C.
981x497mm (96 x 96 DPI)

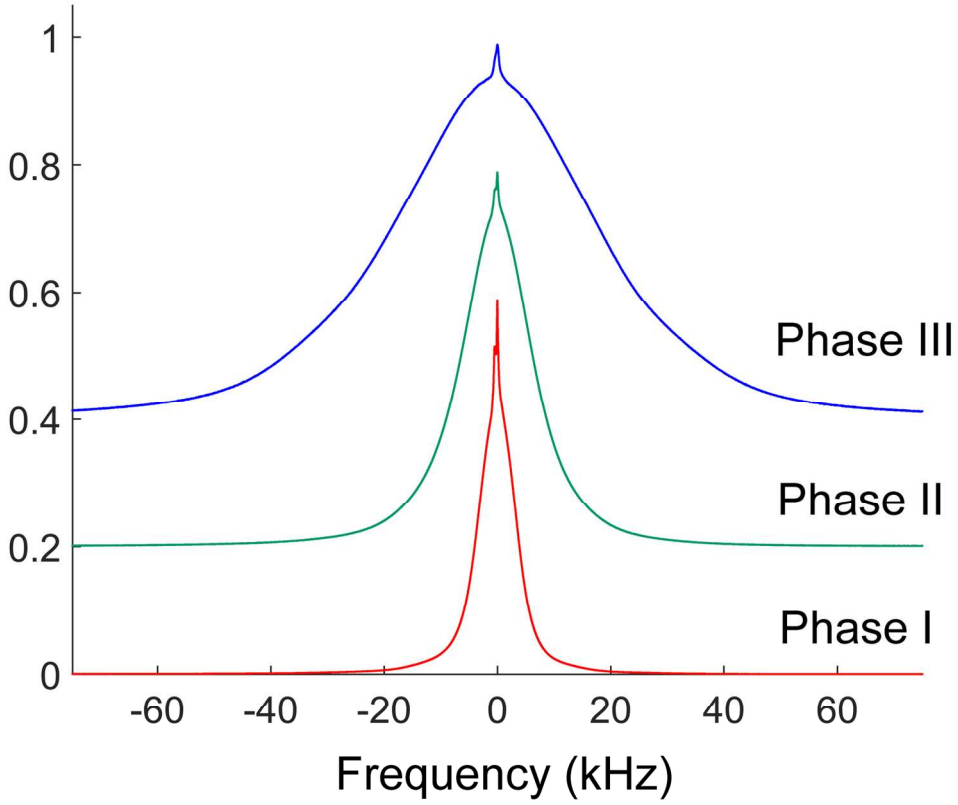

Figure 3. Expansion of ^{1}H NMR spectra of P_{1444}FSI in phases I (34 °C), II (22 °C) and III (-2 °C). Each spectrum is scaled by its maximum intensity.
150x121mm (300 x 300 DPI)

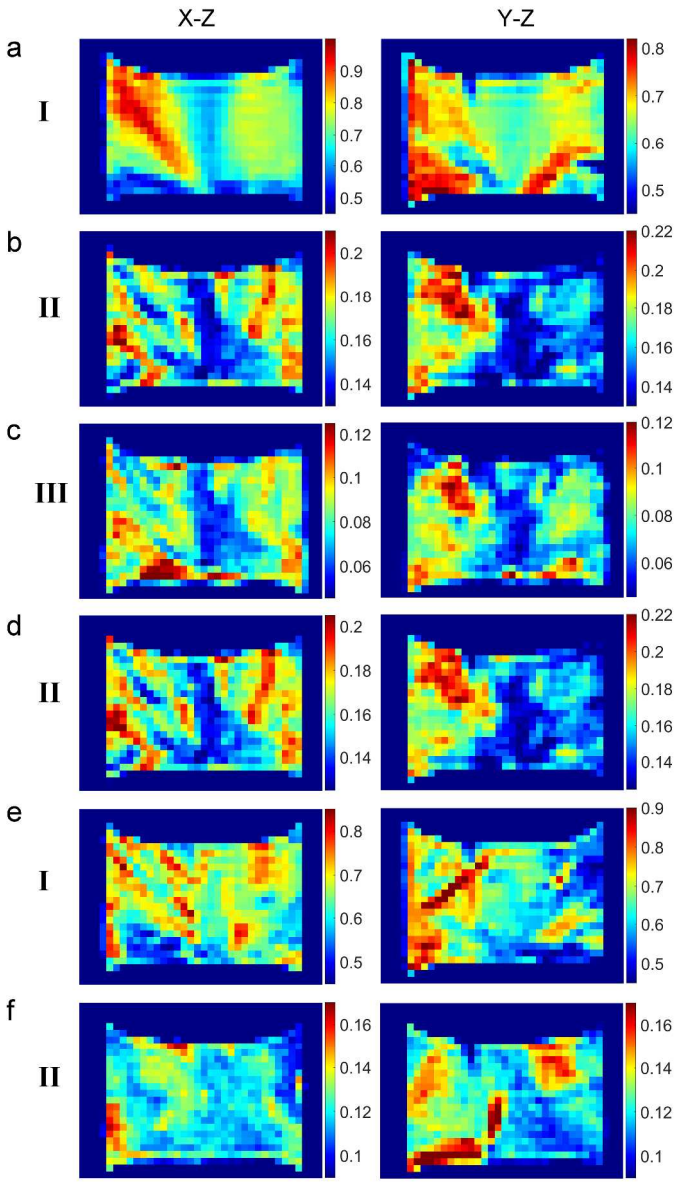

Figure 4. Longitudinal slices (X-Z and Y-Z) through 3D ^{1}H SPRITE images of the P_{1444}FSI sample in phases I - III in the following order: Melt (50 °C) → I (28 °C) (a) → II (18 °C) (b) → III (6 °C) (c) → II (18 °C) (d) → I (28 °C) (e) → II (18 °C) (f); FOV = 17×12.4 mm^2.
823x1458mm (96 x 96 DPI)

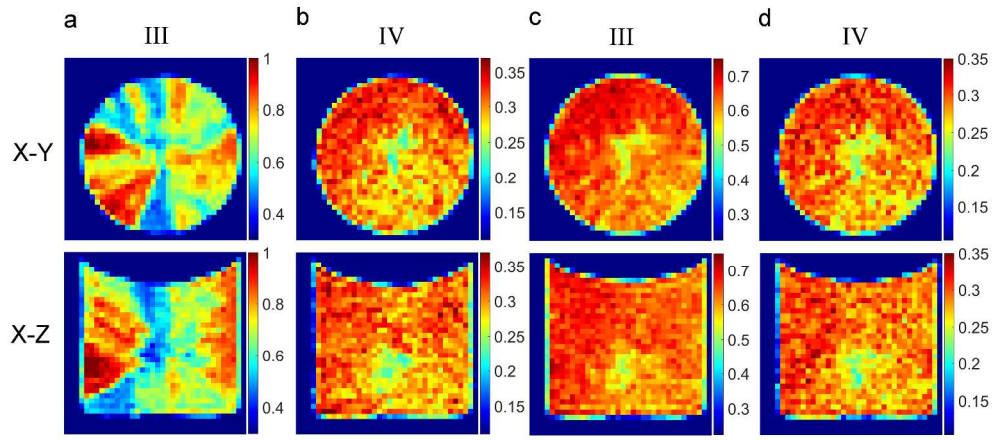

Figure 5. Representative slices (X-Y – top and X-Z - bottom) through 3D ^{19}F SPRITE images of the $P_{1224}PF_6$ sample in phases III and IV in the following order: Melt (150 °C) → I (125 °C) → II (100 °C) → III (30 °C) (a) → IV (16 °C) (b) → III (30 °C) (c) → IV (16 °C) (d); FOV = 17×17 mm^2.
1150x518mm (96 x 96 DPI)

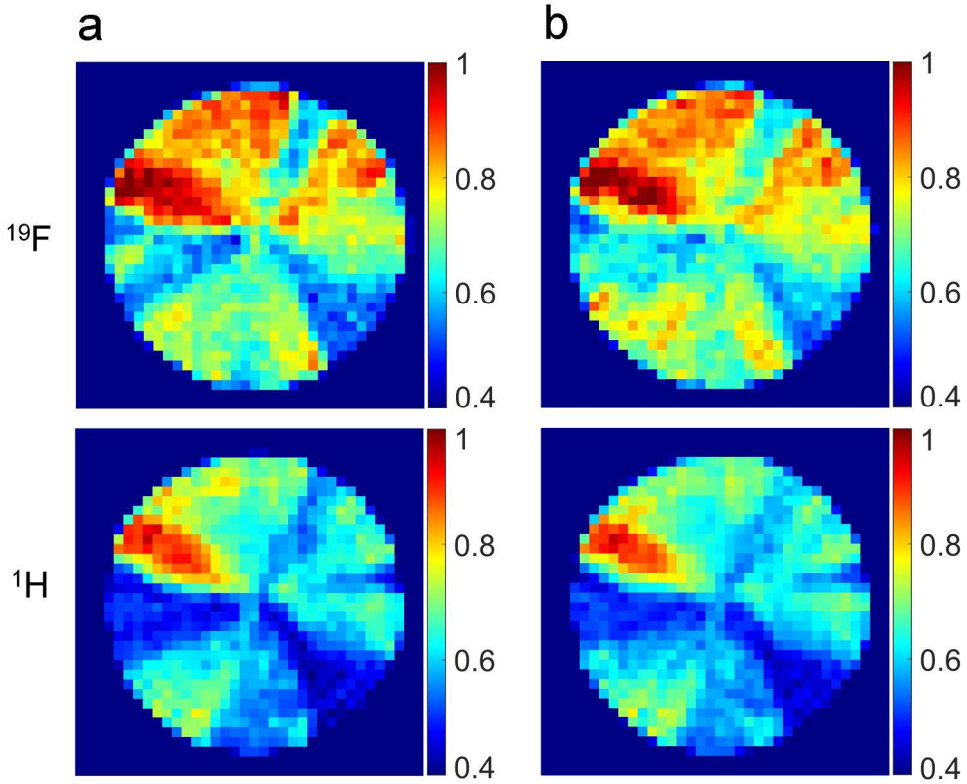

Figure 6. Transverse slices (X-Y) through 3D ^{19}F (top) and ^{1}H (bottom) SPRITE images of the $P_{1224}PF_6$ sample in phase III in the following order: Melt (150 °C) → I (125 °C) → II (100 °C) → III (30 °C) (a) → II (100 °C) → III (30 °C) (b); FOV = 17×17 mm^2.
602x493mm (96 x 96 DPI)

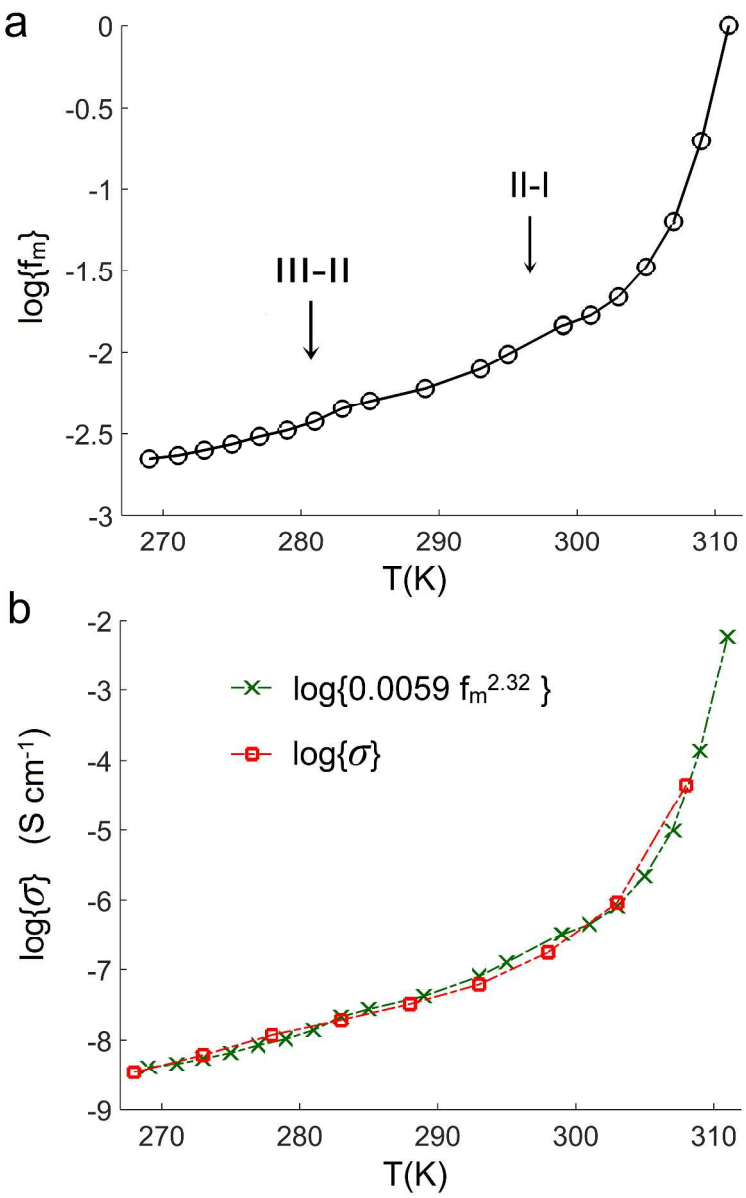

Figure 7. (a) Mobile fractions, log{f_m(T)}, obtained with ^{1}H NMR spectroscopy for P_{1444}FSI. (b) EIS conductivity data, log {σ(T)}, and the corresponding correlation $\sigma(f_m) = 0.0059\ f_m^{2.32}$.
1270x1905mm (96 x 96 DPI)

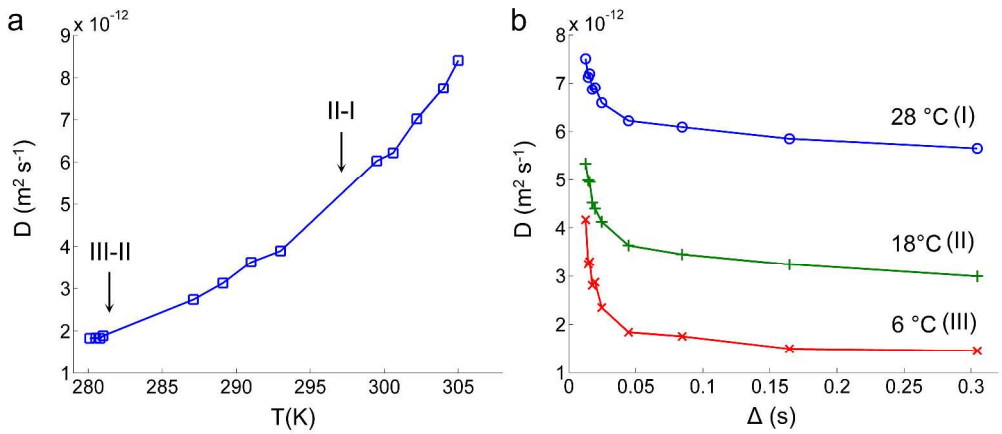

Figure 8. (a) PFG ^{1}H NMR diffusivity, D(T), of the mobile component at Δ = 45 ms. (b) D(Δ) in phases I (28 °C), II (18 °C) and III (6 °C) of $P_{1444}FSI$.
2297x997mm (96 x 96 DPI)

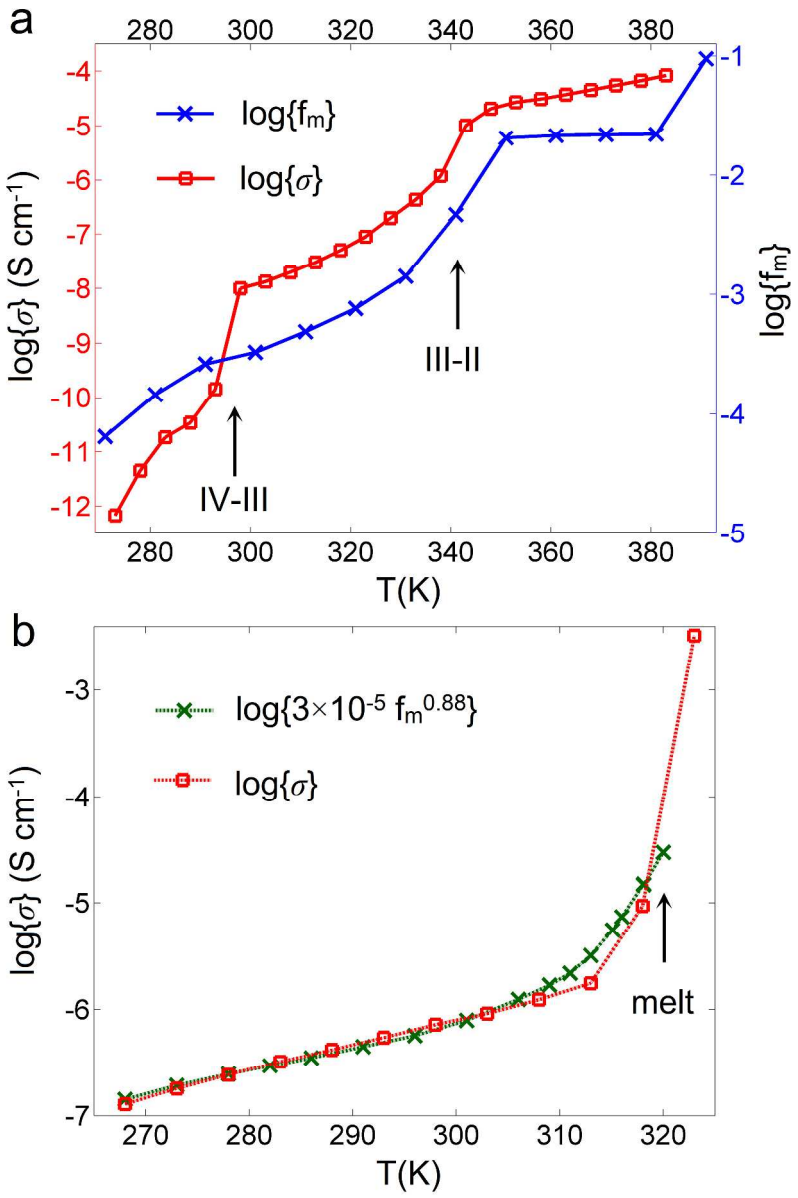

Figure 9. (a) Mobile fractions, log{f_m(T)}, obtained with ^{1}H NMR and EIS conductivity data, log {σ(T)}, for $P_{1224}PF_6$. (b) EIS conductivity data, log {σ(T)}, and the corresponding correlation $\sigma(f_m) = 3\times10^{-5}\ f_m^{0.88}$ observed in phase I of $P_{1222}FSI$.
1058x1587mm (96 x 96 DPI)